
BEV-LANEDET: FAST LANE DETECTION ON BEV GROUND

A PREPRINT

Ruihao Wang
wangruihao@haomo.ai

Jian Qin
qinjian@haomo.ai

Kaiying Li
likaiying@haomo.ai

Dong Cao
caodong@haomo.ai

October 24, 2022

ABSTRACT

Recently, 3D lane detection has been an actively developing area in autonomous driving which is the key to routing the vehicle. However, the previous work did not balance performance and effectiveness. This work proposes a deployment-oriented monocular 3D lane detector with only naive CNN and FC layers. This detector achieved state-of-the-art results on the Apollo 3D Lane Synthetic dataset and OpenLane real-world dataset with 96 FPS runtime speed. We conduct three techniques in our detector: (1) *Virtual Camera* eliminates the difference in poses of cameras mounted on different vehicles. (2) *Spatial Transformation Pyramid* as a light-weighted front-view to bird-eye view transformer can utilize multiscale image-view featmaps. (3) *YOLO-Style Representation* makes a good balance between bird-eye view resolution and runtime speed, and it can reduce the inefficiency caused by the class imbalance due to the sparsity of the lane detection task during training. Experimental results show that our work outperforms state-of-the-art approaches by 10.6% F1-Score on OpenLane dataset and 4.0% F1-Score on Apollo 3D synthetic dataset and with speed of 96 FPS. The source code will release at https://github.com/hm-gigo-team/bev_lane_det.

Keywords 3D lane detection, Autonomous driving, Bird-eye-view

1 Introduction

In recent years, autonomous driving technology has become increasingly popular in industry and academia. As one of the fundamental guarantees for autonomous driving, lane detection has also received much attention from researchers. Robust lane detection in real-time is one of the foundations for advanced autonomous driving, which can provide lots of useful information for ADS (Autonomous Driving Systems), vehicle self-control, localization, and map construction.

Existing lane detection methods can be divided into two types. The majority work consider lane detection as an 2D-task driven by image caught by forward-facing camera, which are based on segmentation. [5, 25, 22, 20]. In post-processing, the output of the 2D lane detection model is usually projected to the ground plane by IPM (Inverse Perspective Transformation) using the camera intrinsic and extrinsic parameters, and then curve fitting is performed to obtain the lane lines based on the vehicle-ego coordinate system. Based on the ideal case of ground plane hypothesis, the output of 2D methods can get the lane lines similar to real 3D lane lines in the vehicle-ego coordinate system after IPM transformation. **However, this approach can cause other problems in the actual driving process [1, 22], resulting in inaccurate 3D lane lines in the vehicle-ego coordinate system and inaccurate vehicle control. For example, on real roads, uphill and downhill scenarios are frequent. In such scenarios, the 2D lane methods + IPM approach generates incorrect 3D lane predictions, causing the vehicle in autonomous driving to have incorrect driving behavior.**

In order to overcome these problems and make the lane detection in autonomous driving an industrial-grade product application, more recent research [10, 8, 11, 17, 3] have focus on the more complex 3D lane perception domain. 3D-LaneNet [10] proposes an end-to-end approach from 2D image space to orthographic bird's eye view space (BEV). The method unifies 2D image feature encoding, spatial transformation and 3D lane extraction. Recent sota work, performer [3] proposes a framework that unifies the detection tasks of 2D lane lines and 3D lane lines. The work also proposes spatial transformation module, Perspective Transformer to obtain excellent 3D lane detection, and also publish a large-scale real scene based 3D dataset, OpenLane. The achievements of these work are remarkable and have shown that it is extremely feasible to regress 3D lane detection directly from monocular images using a single model.

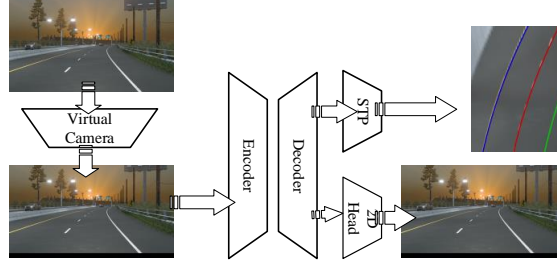


Figure 1: Conceptual diagram of our approach

In this paper, we introduce BEV-LaneDet, a robust and real-time framework that achieves 3D lane detection from single image shown in Figure. We establish *Virtual Camera* to unify the intrinsic and extrinsic parameters of front-facing cameras in different vehicles by homography method[7]. This module guarantees the consistency of the spatial relationship of front-facing cameras in different vehicles. After applying *Virtual Camera* in 2D image, there is no need to incorporate intrinsic and extrinsic parameters for features in both the training and inference phases. Moreover, inspired by ASPP[4], we present *Spatial Transformation Pyramid*, a light-weighted module based on MLP transforms multiscale front-view featmaps to bird-eye-view, which can provide robust bird-eye-view features for 3D lane detection. Inspired by [29, 23], we propose *YOLO-Style Representation module* as our lane anchor representation. We demonstrate that is uncomplicated and effective module to represent 3D lanes in the bird-eye-view plane. In our experiments, we perform extensive studies to confirm that our BEV-LaneDet significantly outperforms the previous state-of-the-art [3] in terms of F-score, by up to nearly 10% in OpenLane test set.

2 Related Work

2D Lane Detection. In recent years, there have been impressive developments in the area of 2D lane detection using deep neural networks, thanks to the effectiveness of CNN models. In the 2D lane detection, it is divided into three directions, pixel-wise segmentation, row-wise segmentation, and curve parameters. [25, 34] consider 2D lane detection as a multi-category segmentation task based on pixel-wise, these methods set the limit number of lane lines, and the computing cost is expensive. 2D lane detection is also regarded as two-class segmentation by [18, 22], and then combines with the embedding way to cluster each lane line to achieve the variable number of lane detection. [27, 20, 33] focus on the row-wise level to detect the 2D lane lines. By setting the row-anchor in the row direction and setting the grid cell in the column direction to model the 2D lane lines on the image space, row-wise methods greatly improve the speed of inference. [9, 31] argue that the lane line can be fitted by specific curve parameters on the 2D image space. So it is proposed that the 2D lane detection can be converted into the problem of curve parameters regressing by detecting starting point, ending point and curve parameters. However, these methods based on 2D image need to combine camera intrinsic and extrinsic parameters for IPM projecting to the ground in post-processing, which are based on the ideal situation of the ground plane hypothesis. As mentioned in Chapter 1, in the actual driving process, 2D lane detection + IPM is difficult to get the exact position of the real lane line.

BEV Lane Detection. In order to obtain more accurate road cognition results, much works have turned their attention to lane detection in 3D space. [10, 11, 3, 17] use sota results to prove the feasibility of using CNN network for 3D lane detection in monocular images. [10] introduces a unified network for encoding 2D image information, spatial transform and 3D lane detecton in two path-ways: the Image-View pathway encodes features from 2D image, while the Top-view pathway provides translation-invariant features for 3D lane Detection. [11] proposes an extensible two-stage framework, which separates the image segmentation sub-network and the geometry encoding sub-network. The specific method is to train the 2D lane segmentation part separately, and combine the camera intrinsic and extrinsic parameters to convert the 2D segmentation mask to IPM project into virtual top-view, and then perform anchor-based 3D lane detection in the virtual top-view. [3] proposes a unified 2D lane detection and 3D lane detection framework, and introduces trasformer into the spatial transformation module to obtain more robust feature expression, which is the current sota in the direction of 3D lane detection, and proposes a real scene based Large-scale annotated 3D lane dataset, OpenLane.

Spatial Transform. A key module of 3D lane detection is the spatial transformation from 2D feature to 3D feature. The spatial transform module[14] is a trainable module that is flexibly inserted into the CNN to implement the corresponding spatial transformation of the input feature map, and is suitable for converting 2D space feature into 3D geometric feature information. In the 3D lane detection, there are four kinds of commonly used spatial transform modules, such as

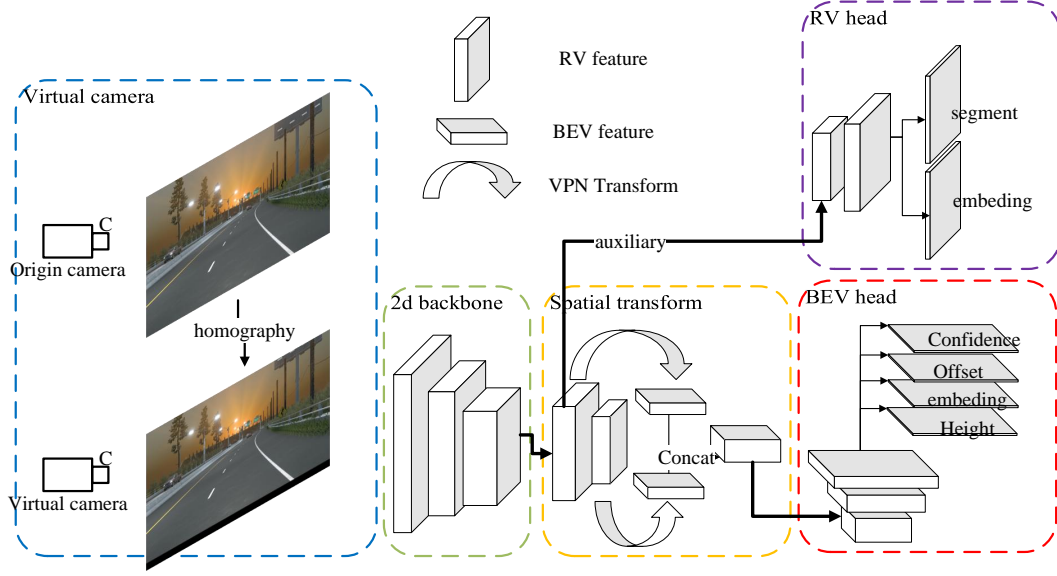


Figure 2: Our network structure consists of five parts: Virtual Camera, Spatial Transformation Pyramid, Yolo Style Head, Front View Auxiliary Supervision

IPM-based methods [30, 10, 11], but this method relies strongly on the camera intrinsic and extrinsic parameters and ignores the ground surface undulations and vehicle shaking. **The MLP-based method** [24, 18] has robust performance and is easy to deploy, but it is a fixed spatial mapping, which are difficult to be integrated with the camera intrinsic and extrinsic parameters. **Transformer-based** spatial transformation module[3, 19] has better robustness, but it is not easy to deploy due to the large amount of computation. **The space transformation based on depth**[26, 13] has a large amount of calculation and thus is not suitable for deployment.

In view of the issue above, we propose our 3D lane detection method, which has three contributions. Firstly, we introduce a data preprocessing module based on virtual camera, with transforms the various cameras with different intrinsic and extrinsic parameters into a unified camera by homography matrix[7]. Experiments show that this module has better allowed the network to extract the robust features of 2D images. Second, a pyramid module based on MLP spatial transformation is proposed. The above mentioned MLP spatial transformation performance is robust and easy to deploy. Inspired by ASPP[4], we also add the concept of spatial feature pyramid. Experiments show that this method is very effective. Combined with the excellent work in target detection [29, 32, 35], different from the way of constructing anchors in [16, 28, 10, 3], we propose to add bin+offset to 3D lane detection. We find that these methods can better reduce the y-error and make the 3D lane detection more robust through experiments in OpenLane and Apollo dataset.

3 Methodology

As show in Figure.2, the whole network architecture consists of four parts:

- *Virtual Camera*: preprocessing of unified camera’s intrinsic and extrinsic parameters.
- *Front View Backbone*: the front view feature extractor.
- *Spatial Transformation Pyramid*: Projecting front view features to bird-eye-view features.
- *YOLO-Style Representation*: Head of detector base on YOLO[29].

As show in Figure.2. Firstly, The input images are projected by their intrinsic and extrinsic parameters to *Virtual Camera* with fixed intrinsic and extrinsic parameters. This process allows for quick harmonization of the intrinsic and extrinsic parameters of the front cameras on different vehicles. Then we use a front view feature extractor to extract the features of front view image. We carried out experiments with ResNet18 and ResNet34 respectively[12]. **In order to better promote the network to extract front view features, front view lane auxiliary supervision is added to the output part of the backbone network.** Inspire by [4], Then we design a fast multi-scale spatial transformation module based on [24], which we call *Spatial Transformation Pyramid*. This module is responsible for spatial transformation from front view features to BEV features. Finally, we predict the lane on the plane tangent to the local road surface P_{road} and

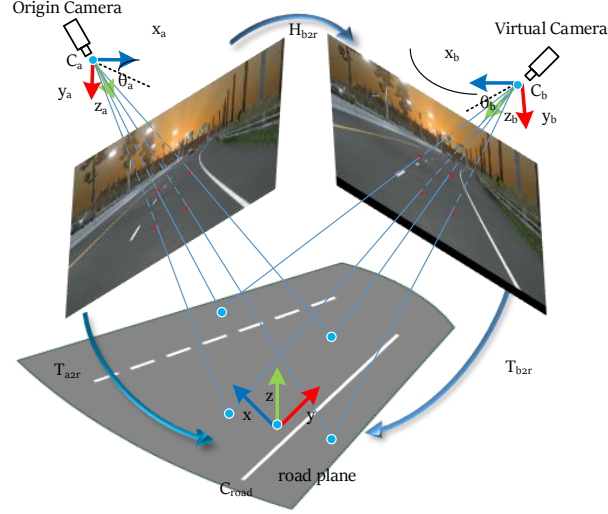


Figure 3: Schematic diagram of the *Virtual Camera*. The core of the *Virtual Camera* is that current camera and virtual camera co-planar on P_{road} after inverse-perspective mapping(IPM)

P_{road} is the plane with $z = 0$ in the road coordinates $C_{road} = (x, y, z)$. We divide the P_{road} into several cells, one of which represents an area of $x \times x$ (x defaults to $0.5m$). Inspired by the YOLO[29] and LaneNet[22], we predict the confidence, the embedding used for clustering, the offset from the cell center to the lane in row direction and the average height of each cell. In the inference, We use a fast clustering method to fuse the results of each branch into lanes.

3.1 Preprocessing of unified camera’s intrinsic and extrinsic parameters

The intrinsic and extrinsic parameters of different vehicles are different, which has a great influence on the results of the model. Different from the method of integrating the camera’s intrinsic and extrinsic parameters into the network [3, 26], we realize a preprocessing method of quickly unifying the camera’s intrinsic and extrinsic parameters by establishing a *Virtual Camera* with fixed intrinsic and extrinsic parameters.

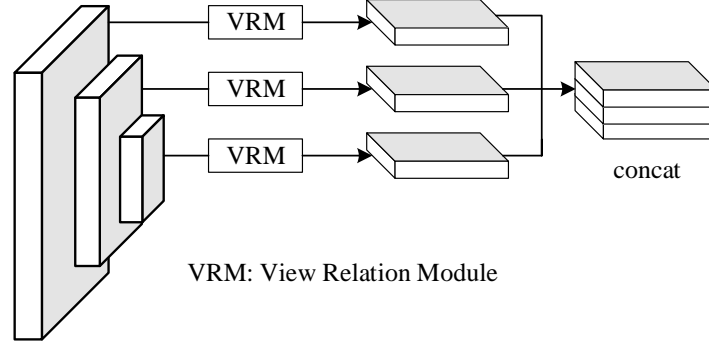
We assume that P_{road} be the plane tangent to the local road surface. Because the BEV lane detection task pays more attention to the plane P_{road} . We use the coplanarity of homography to project the image of current camera to image of the *Virtual Camera* through the homography matrix $H_{i,j}$. Therefore, the *Virtual Camera* with fixed intrinsic and extrinsic parameters is used to unifying the intrinsic and extrinsic parameters of the cameras.

$$H_{i,j}u_i^k = u_j^k \quad (1)$$

As show in Figure.3, The intrinsic parameters K_i and extrinsic parameters (R_i, T_i) of the *Virtual Camera* are fixed, which are derived from the mean value of the intrinsic and extrinsic parameters of the dataset. In the training and inference stage of the network, the homography $H_{i,j}$ is calculated according to the camera’s intrinsic parameters K_j and extrinsic parameters (R_j, T_j) provided by the current camera and the intrinsic and extrinsic parameters of the *Virtual Camera*. We refer [2] to calculate $H_{i,j}$. Firstly, select four points $x^k = (x^k, y^k, 0)^T$ where $k = 1, 2, 3, 4$ on the BEV plane P_{road} and project them to the image of current camera and image of *Virtual Camera* respectively to obtain $u_i^k = (u_i^k, v_i^k, 1)^T$ and $u_j^k = (u_j^k, v_j^k, 1)^T$. Secondly, $H_{i,j}$ is obtained by least square method. as show in Eqn.1.

3.2 MLP Based Spatial Transformation Pyramid

Because spatial transformation based on depth-based[26, 13], transformer-based[3, 19] and other methods are computationally expensive and unfriendly to autopilot chips, our spatial transformation modelule is based on MLP[24] which is called *View Relation Module*. *View Relation Module* use a view relation module R to learn the relations between the any two pixel positions in flattened first-view feature map and flattened top-down-view feature map. However, *View Relation Module* did not perform well in previous work because camera’s parameters can not incorporated into it. And *View Relation Module* is sensitive to the position of the front view feature layer. Therefore, we designed the *Virtual Camera* to unify the intrinsic and extrinsic parameters of the camera. Meanwhile, our work analyzes the effect of resolution of front-view features doing spatial transformation by *View Relation Module*. Low resolution features

Figure 4: Schematic diagram of the *Spatial Transformation Pyramid*

are found to be more suitable for spatial transformation by *View Relation Module* through experiments. We speculate that the low resolution features contain more global information. And since the MLP-based spatial transformation is a fixed mapping, the low-resolution features are easier to learn. Inspired by the DeepLab[4], we designed a *Spatial Transformation Pyramid* based on *View Relation Module*. We use 1/64 resolution feature of the input image $s64$ and 1/32 resolution feature of the input image $s32$ to do spatial transformation respectively, and then concatenate the results of both.

$$f_t[i] = \text{concat}(R_i^{s32}(f^{s32}[1], \dots, f^{s32}[HW^{s32}]), R_i^{s64}(f^{s64}[1], \dots, f^{s64}[HW^{s64}])) \quad (2)$$

where R_i^{s32} denotes *View Relation Module* of $s32$, R_i^{s64} denotes *View Relation Module* of $s64$, $f_t[i]$ denote pixel on bev feature.

3.3 YOLO-Style Representation

The representation of 3D lane has a significant impact on the results of 3D lane detection. Most of the previous methods are based on 3D anchor to represent 3D lanes[3, 10, 11]. However, 3D anchor design is difficult and ineffective. Different from 3D anchor and other design methods, we propose a method to predict 3D lanes in the bird-eye-view plane by referring to the YOLO[29] and LaneNet[22]. As shown in Figure.5, we divide the BEV plane P_{road} which is the plane with $z = 0$ in the road coordinates $C_{road} = (x, y, z)$ into several cells. Each cell represents $x \times x$ (x defaults to $0.5m$). We directly predict the four heads with the same resolution, including the confidence, the embedding used for clustering, the offset from the cell center to the lane in row direction and the average height of each cell. Unlike YOLO, we get uncoupled heads.

Size of the grid cell has a great influence on the prediction results. Too small a grid cell size affects the balance of positive and negative samples in the confidence branch. However, if the cell size is too large, the embedding of different lanes will overlap. Considering the sparsity of lane tasks, we recommend that the grid cell size be $0.5 \times 0.5m^2$ through experiments. In training and inference, we predict the lanes of $(-10m, 10m)$ in the y direction and $(3m, 103m)$ in the x direction in the road coordinates $C_{road} = (x, y, z)$. So four 200×40 resolution tensor, **including confidence, embedding, offset and height are output from the BEV lane detection head.** The Confidence head, embedding head, and offset head generates the instanced lanes under the BEV, as show in Fig. 5.

3.3.1 Confidence

Similar to YOLO[29], the confidence of lanes is a binary branch. Each pixel represents the confidence of the cell containing lanes. We interpolate the lanes in the visible area of the training data. If there is a lane through the cell, the confidence scores should be one, otherwise the confidence scores should be zero. The confidence loss can be expressed by Binary Cross Entropy loss.

$$L_{conf}^{3d} = \sum_i^{s1 \times s2} (\hat{p}_i \log p_i + (1 - \hat{p}_i) \log(1 - p_i)) \quad (3)$$

where p_i denotes probability of the confidence predicted by the model and \hat{p}_i denotes ground truth of confidence.

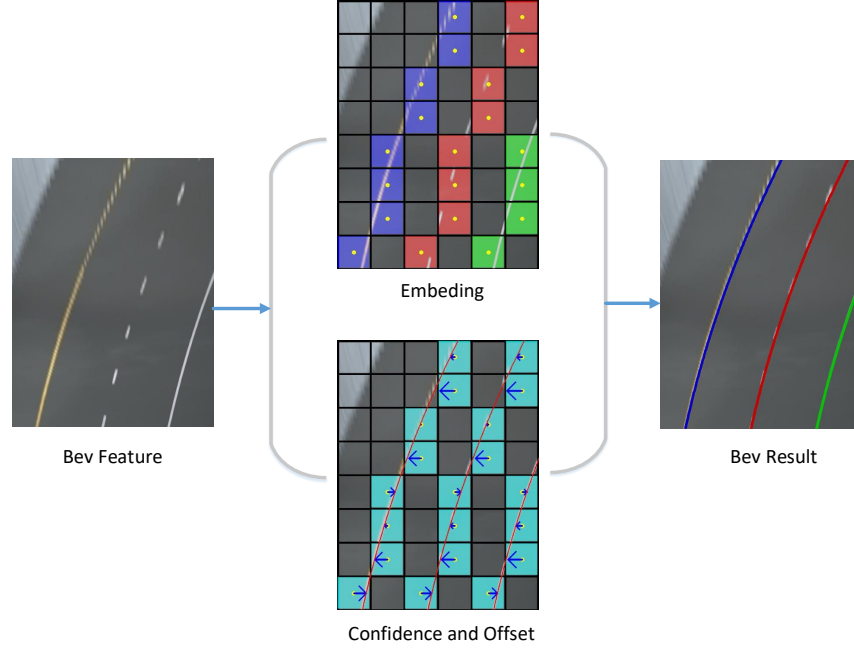


Figure 5: Schematic diagram of the *YOLO-Style Representation*. The BEV plane P_{road} is divided into $s1 \times s2$ grids. Each grid represents an area of $x \times xm^2$. Bev features are convolved to obtain three branch, including the embedding, confidence and offset of each grid. The three branch merge the instantiated lane lines under the clustering BEV plane

3.3.2 Offset

Since confidence branch does not accurately represent the exact location of lanes, offset branch is responsible for predicting the offset from the cell center to the lane in the y direction in the road coordinates $C_{road} = (x, y, z)$. As shown in Fig. 5, similar to YOLO, the model predicts the offset of each cell Δy_i . The offset is normalized by Sigmoid and subtracted by 0.5 so that the predicted range of offset is $(-0.5, 0.5)$. The offset loss can be expressed by MSE loss. Note that we only calculate offset for grid cells with positive ground truth of confidence.

$$L_{offset}^{3d} = \sum_i^{s1 \times s2} 1_{obj} (\sigma(\Delta y_i) - \Delta \hat{y}_i)^2 \quad (4)$$

where 1_{obj} denotes if lane through this cell. Δy_i denotes offset from prediction and $\Delta \hat{y}_i$ denotes offset from the ground truth.

3.3.3 Embedding

To distinguish the lane identity of each pixel in the confidence branch, we predicted the embedding feature of each grid cell with reference to [6, 22]. In the training of the network, based on distance metric learning, the distance between cell embeddings belonging to the same lane is small, whereas the distance between cell embeddings belonging to different lanes is maximized. In the inference of the network, we use a fast unsupervised clustering post-processing method to predict the variable number of lanes. Unlike front-view lanes that usually converge at vanishing point, 3D lane is more suitable for the embedding clustering loss function.

$$L_{embed}^{3d} = L_{var}^{3d} + L_{dist}^{3d} \quad (5)$$

where L_{var}^{3d} denotes loss of minimizing the mean of cell embeddings belonging to the same lane. L_{dist}^{3d} denotes loss of maximizing the variance of cell embeddings belonging to the different lanes.

3.3.4 Height of lane

Because our task is to predict 3D lanes, confidence, offset and embedding can only predict the x and y of key points in the road coordinates $C_{road} = (x, y, z)$, so the height branch is responsible for predicting the height of lane z of the key

Table 1: Comparison with other open-sourced 3D methods on OpenLane. Our method achieves the best F1-Score on the entire validation set and every scenario set

Method	All	Up&down	Curve	Extreme weather	Night	Intersection	Merge&Split
3d-lanenet	40.2	37.7	43.2	43	39.3	29.3	36.5
Gen-lanenet	29.7	24.2	31.1	26.4	19.7	19.7	27.4
Persformer	47.8	42.4	52.8	48.7	37.9	37.9	44.6
Ours	58.4	48.7	63.1	53.4	53.4	50.3	53.7

points of the 3D lane in the road coordinates $C_{road} = (x, y, z)$. In the training phase of the network, we use the average height in a grid cell as the ground truth of the lane height. At the same time, similar height branch, Only the grid cells with positive ground truth of confidence are counted in the loss.

$$L_{height}^{3d} = \sum_i^{s1 \times s2} 1_{obj} (h_i - \hat{h}_i)^2 \quad (6)$$

where h_i denotes the height of the grid cell predicted by the model and \hat{h}_i denotes height of the grid cell from ground truth.

3.3.5 Total loss

The total loss includes 3D lane loss and front view lane loss. The front view lane loss includes lane segmentation loss of front view and lane clustering loss of front view, which we refer to LaneNet[22].

$$L_{total} = \lambda_{conf}^{3d} L_{conf}^{3d} + \lambda_{embed}^{3d} L_{embed}^{3d} + \lambda_{offset}^{3d} L_{offset}^{3d} + \lambda_{height}^{3d} L_{height}^{3d} + \lambda_{seg}^{2d} L_{seg}^{2d} + \lambda_{embed}^{2d} L_{embed}^{2d} \quad (7)$$

where L_{seg}^{2d} denotes lane segmentation loss of front view and L_{embed}^{2d} denotes lane embedding loss of front view.

3.3.6 Inference

In the inference phase, the four branches of the network output, including confidence M_{conf} , embedding M_{emb} , offset M_{off} and lane height M_Z , are synthesized into instance-level lane by a fast unsupervised clustering which we refer to mean-shift. As show in Alg. 1. this process consists of four steps.

- Filtering the point of confidence mask M_{conf} by $S_{threshold}$ to get the E_{list} .
- Clustering points of M_{emb} to get the R_{point} and R_{center} by Inter-class distance D_{gap} .
- Adding offset M_{off} and lane height M_Z to points in each lane to get R_{lines}
- Fit the key points of the lane to get the lane equation R_{fit} .

4 Experiments

In order to verify the performance of our work, our model is tested on the real-world data openlane dataset [3] and the simulation dataset apollo dataset[11]. Compared with previous methods, including Persformer[3], reconstruction from top view[17], Gen-Lanenet[11], 3D-Lanenet[8], CLGO[21] etc., it is proved that our work can reach the level of state-of-the-art on F1-score and achieve competitive results on X/Z error.

4.1 Evaluation Metrics and Implementation Details

Our evaluation metrics are followed by Gen-Lanenet[11] on both 3D datasets, which include F1-score in different scenes and X/Z error in different areas.

4.2 Results on OpenLane

Openlane contains 150000 training data and 40000 test data. In order to verify the performance of the model on every scene, the Up&Down case, Curve case, Extreme Weather case and Night are split from the verification set case,

Table 2: Comprehensive 3D Lane evaluation under different metrics. Our Method outperforms previous 3D methods on the metrics of F1-score and x error far(m).

Method	F-Score	X error near	X error far	Z error near	Z error far
3D-Lanenet	40.2	0.278	0.823	0.159	0.714
Gen-lanenet	29.7	0.309	0.877	0.16	0.75
Persformer	47.8	0.322	0.778	0.213	0.681
Ours	58.4	0.309	0.659	0.244	0.631

Table 3: There is results of different models on Apollo 3D Lane Synthetic. Compared with 3D-Lanenet[8], Gen-lanenet[11], 3D-lanenet(1/att)[15], Gen-lanenet(1/att)[15], CLGO[21], Reconstruct from top[17], Persformer[3], our model is the best on F1-score and x error

Scene	Method	F-Score	X error near	X error far	Z error near	Z error far
Balanced Scence	3D-Lanenet	86.4	0.068	0.477	0.015	0.202
	Gen-lanenet	88.1	0.061	0.496	0.012	0.214
	3D-lanenet(1/att)	91	0.082	0.439	0.011	0.242
	Gen-lanenet(1/att)	90.3	0.08	0.473	0.011	0.247
	CLGO	91.9	0.061	0.361	0.029	0.25
	Reconstruct from top	91.9	0.049	0.387	0.008	0.213
	Persformer	92.9	0.054	0.356	0.01	0.234
	Ours	96.9	0.016	0.242	0.02	0.216
Rarely Observed	3D-LaneNet	72	0.166	0.855	0.039	0.521
	Gen-LaneNet	78	0.139	0.903	0.03	0.539
	3D-LaneNet(1/att)	84.1	0.289	0.925	0.025	0.625
	Gen-LaneNet(1/att)	81.7	0.283	0.915	0.028	0.653
	CLGo	86.1	0.147	0.735	0.071	0.609
	Reconstruct from top	83.7	0.126	0.903	0.023	0.625
	Persformer	87.5	0.107	0.782	0.024	0.602
	Ours	97.6	0.031	0.594	0.04	0.556
Vivual Variants	3D-LaneNet	72.5	0.115	0.601	0.032	0.23
	Gen-LaneNet	85.3	0.074	0.538	0.015	0.232
	3D-laneNet(1/att)	85.4	0.118	0.559	0.018	0.29
	Gen-LaneNet(1/att)	86.8	0.104	0.544	0.016	0.294
	CLGo	87.3	0.084	0.464	0.045	0.312
	Reconstruct from top	89.9	0.06	0.446	0.011	0.235
	PersFormer	89.6	0.074	0.43	0.015	0.266
	Ours	95	0.027	0.32	0.031	0.256

Intersection case, and Merge&Split case. Table.1 shows the F1-score of the model in every scene. Our model trains 10 epochs in the training set and achieves state-of-the-art in each scences. Table.2 shows the specific performance in F1-score, X/Z error in different work. Our results are 10.6% higher on the F1-score than the previous state-of-the-art work[3]. Since the 3D ground truth of openlane is synthesized by lidar, our work does not show much advantage on X error. However, our work shows a great advantage on X error for the Apollo dataset[11].

4.3 Results on Apollo 3D Synthetic

The data on Apollo[11] includes 10500 discrete frames of monocular RGB images and corresponding 3D lane ground truth, which are split into three scenes: balanced, rally observed, and visual variation scenes. Each scene contains independent training sets and test sets. It should be noted that because our virtual camera needs to use the external parameters of the camera, Apollo does not provide specific external parameters of the camera. We calculate the intrinsic and extrinsic parameters of the camera through the height and pitch of camera provided by the dataset. In Table.3, we give a comparison between the work of the foreword and our work. Our model has trained 80 epochs on these datasets. The results of our work for F1-score and X error both reached the state-of-the-art on apollo. However, because we work more focused on the BEV plane, our work does not perform well on Z error. We will improve this shortcoming in the future.

Table 4: Ablative Study on Openlane. VC: Virtual Camera. STP: Spatial Transform Pyramid. YSR: YOLO-Style Representation

Method	F-score	X error near	X error far	Z error near	Z error far
Baseline(ResNet34)	48.7	0.376	0.791	0.265	0.713
+ virtual camera	53.3	0.324	0.695	0.330	0.705
+ 2d det	54.5	0.338	0.689	0.258	0.614
+ STP	55.7	0.321	0.701	0.253	0.624
+ YSR without offset	57.9	0.429	0.734	0.243	0.630
+ offset(BEV-LaneDet)	58.4	0.309	0.659	0.244	0.631
BEV-LaneDet(ResNet18)	57.8	0.318	0.705	0.245	0.629

Table 5: Influence of cell size and offset on results

Method	F-score	X error near	X error far	Z error near	Z error far
0.05m without offset	43.2	0.345	0.770	0.261	0.700
0.2m without offset	55.7	0.321	0.701	0.253	0.624
0.5m without offset	57.9	0.429	0.734	0.243	0.630
0.5m with offset	58.4	0.309	0.659	0.244	0.631
1m without offset	56.8	0.607	0.856	0.241	0.593
1m with offset	57.7	0.317	0.671	0.245	0.590

4.4 Ablation Study

The experiment in this section will be carried out on Openlane, and the evaluation metrics is still based on Gen-Lanenet[11]. We put $0.2 \times 0.2m^2$ per grid cell, VRM[24] to do spatial transformation, and without Virtual Camera method as the baseline. We prove the effectiveness of our methods by adding three methods: *Virtual Camera*(VC), *Spatial Transformation Pyramid*(STP), and *YOLO-Style Representation*(YSR) on Table. 4.

In addition, we also compared the effects of different backbones and 2D auxiliary supervision on the experimental results. At the same time, in order to verify the influence of different output resolutions on YOLO-Style Representation, we added a Table. 5. In the experiment without offset, the F1-score of the lane keeps growing as the grid size grows. However, as the grid gets larger, X error also gets larger. When offset is added, x error returns to the normal level for the large grid.

5 Conclusions and Outlook

In this paper, we have proposed BEV-LaneDet, a fast, robust and effective 3D lane detector on BEV plane. we propose *Virtual Camera* to guarantee the consistency of the spatial relationship of front-facing cameras in different vehicles, and we have proven its effectiveness through experiments. Moreover we demonstrate experimentally that *Spatial Transformation Pyramid*, which is a module we propose for spatial transformation, is effective. Finally, we propose the *YOLO-Style Representation*, which predicts 3d lanes directly on the BEV plane, with both speed and effect. Finally, we believe that the BEV-LaneDet can facilitate additional on-road 3D tasks such as 3D vehicle detection.

Algorithm 1 Post-processing algorithm of our method

Input: $M_{conf}, M_{emb}, M_{off}, M_Z \leftarrow Model(I_v)$;
Output: Lane lines after fitting, R_{fit}

- 1: Filtering the point of confidence mask by $S_{threshold}$ to get the E_{list} :
- 2: **for** $x = 0; x < M_{conf}.cols; x++$ **do**
- 3: **for** $y = 0; y < M_{conf}.rows; y++$ **do**
- 4: **if** $M_{conf}[x, y] \geq S_{threshold}$ **then**
- 5: $E_{list}.append([x, y, M_{emb}[:, y, x]])$;
- 6: **end if**
- 7: **end for**
- 8: **end for**
- 9: Clustering points to get the R_{point} and R_{center} by D_{gap} :
- 10: **for** $i = 0; i < E_{list}.length; i++$ **do**
- 11: $x, y, value = E_{list}[i]$;
- 12: $min_gap = D_{gap} + 1$;
- 13: $min_cid = -1$;
- 14: **for** $j = 0; j < R_{center}.length; j++$ **do**
- 15: $center_id, (center, num) = R_{center}[j]$;
- 16: $diff = Euclidean(value, center)$;
- 17: **if** $diff < min_gap$ **then**
- 18: $min_gap = diff$;
- 19: $min_cid = center_id$;
- 20: **end if**
- 21: **end for**
- 22: **if** $min_gap < D_{gap}$ **then**
- 23: $R_{point}.append([x, y, min_cid])$;
- 24: $center, num = R_{center}[min_cid]$;
- 25: $R_{center}[min_cid] = [(center * num + value) / (num + 1), num + 1]$;
- 26: **else**
- 27: $R_{center}.append([value, 1])$;
- 28: $R_{point}.append([x, y, R_{center}.length - 1])$
- 29: **end if**
- 30: **end for**
- 31: Adding offset to points in each line to get R_{lines} :
- 32: **for** $k = 0; k < R_{point}.length; k++$ **do**
- 33: $x, y, id = R_{point}[k]$;
- 34: $off_x, off_y = M_{off}[:, y, x]$;
- 35: $z = M_Z[y, x]$;
- 36: $R_{lines}[id].append([x + off_x, y + off_y, z])$;
- 37: **end for**
- 38: $R_{fit} = FitFunc(R_{lines})$;

References

- [1] Bai, M., Mattyus, G., Homayounfar, N., Wang, S., Lakshmikanth, S.K., Urtasun, R.: Deep multi-sensor lane detection. In: 2018 IEEE/RSJ International Conference on Intelligent Robots and Systems (IROS). pp. 3102–3109. IEEE (2018)
- [2] Baker, S., Datta, A., Kanade, T.: Parameterizing homographies. Robotics Institute, Pittsburgh, PA, Tech. Rep. CMU-RI-TR-06-11 (2006)
- [3] Chen, L., Sima, C., Li, Y., Zheng, Z., Xu, J., Geng, X., Li, H., He, C., Shi, J., Qiao, Y., et al.: Persformer: 3d lane detection via perspective transformer and the openlane benchmark. arXiv preprint arXiv:2203.11089 (2022)
- [4] Chen, L.C., Papandreou, G., Kokkinos, I., Murphy, K., Yuille, A.L.: Deeplab: Semantic image segmentation with deep convolutional nets, atrous convolution, and fully connected crfs. *IEEE transactions on pattern analysis and machine intelligence* **40**(4), 834–848 (2017)
- [5] Cordts, M., Omran, M., Ramos, S., Rehfeld, T., Enzweiler, M., Benenson, R., Franke, U., Roth, S., Schiele, B.: The cityscapes dataset for semantic urban scene understanding. In: *Proceedings of the IEEE conference on computer vision and pattern recognition*. pp. 3213–3223 (2016)
- [6] De Brabandere, B., Neven, D., Van Gool, L.: Semantic instance segmentation with a discriminative loss function. arXiv preprint arXiv:1708.02551 (2017)
- [7] DeTone, D., Malisiewicz, T., Rabinovich, A.: Deep image homography estimation. arXiv preprint arXiv:1606.03798 (2016)
- [8] Efrat, N., Bluvstein, M., Oron, S., Levi, D., Garnett, N., Shlomo, B.E.: 3d-lanenet+: Anchor free lane detection using a semi-local representation. arXiv preprint arXiv:2011.01535 (2020)
- [9] Feng, Z., Guo, S., Tan, X., Xu, K., Wang, M., Ma, L.: Rethinking efficient lane detection via curve modeling. In: *Proceedings of the IEEE/CVF Conference on Computer Vision and Pattern Recognition*. pp. 17062–17070 (2022)
- [10] Garnett, N., Cohen, R., Pe’er, T., Lahav, R., Levi, D.: 3d-lanenet: end-to-end 3d multiple lane detection. In: *Proceedings of the IEEE/CVF International Conference on Computer Vision*. pp. 2921–2930 (2019)
- [11] Guo, Y., Chen, G., Zhao, P., Zhang, W., Miao, J., Wang, J., Choe, T.E.: Gen-lanenet: A generalized and scalable approach for 3d lane detection. In: *ECCV* (2018)
- [12] He, K., Zhang, X., Ren, S., Sun, J.: Deep residual learning for image recognition. In: *Proceedings of the IEEE conference on computer vision and pattern recognition*. pp. 770–778 (2016)
- [13] Huang, J., Huang, G., Zhu, Z., Du, D.: Bevdet: High-performance multi-camera 3d object detection in bird-eye-view. arXiv preprint arXiv:2112.11790 (2021)
- [14] Jaderberg, M., Simonyan, K., Zisserman, A., et al.: Spatial transformer networks. *Advances in neural information processing systems* **28** (2015)
- [15] Jin, Y., Ren, X., Chen, F., Zhang, W.: Robust monocular 3d lane detection with dual attention. In: *2021 IEEE International Conference on Image Processing (ICIP)*. pp. 3348–3352. IEEE (2021)
- [16] Ko, Y., Lee, Y., Azam, S., Munir, F., Jeon, M., Pedrycz, W.: Key points estimation and point instance segmentation approach for lane detection. *IEEE Transactions on Intelligent Transportation Systems* (2021)
- [17] Li, C., Shi, J., Wang, Y., Cheng, G.: Reconstruct from top view: A 3d lane detection approach based on geometry structure prior. In: *Proceedings of the IEEE/CVF Conference on Computer Vision and Pattern Recognition*. pp. 4370–4379 (2022)
- [18] Li, Q., Wang, Y., Wang, Y., Zhao, H.: Hdmapnet: A local semantic map learning and evaluation framework. arXiv preprint arXiv:2107.06307 (2021)
- [19] Li, Z., Wang, W., Li, H., Xie, E., Sima, C., Lu, T., Yu, Q., Dai, J.: Bevformer: Learning bird’s-eye-view representation from multi-camera images via spatiotemporal transformers. arXiv preprint arXiv:2203.17270 (2022)
- [20] Liu, L., Chen, X., Zhu, S., Tan, P.: Condlanenet: a top-to-down lane detection framework based on conditional convolution. In: *Proceedings of the IEEE/CVF International Conference on Computer Vision*. pp. 3773–3782 (2021)
- [21] Liu, R., Chen, D., Liu, T., Xiong, Z., Yuan, Z.: Learning to predict 3d lane shape and camera pose from a single image via geometry constraints. In: *Proceedings of the AAAI Conference on Artificial Intelligence*. vol. 36, pp. 1765–1772 (2022)

- [22] Neven, D., De Brabandere, B., Georgoulis, S., Proesmans, M., Van Gool, L.: Towards end-to-end lane detection: an instance segmentation approach. In: 2018 IEEE intelligent vehicles symposium (IV). pp. 286–291. IEEE (2018)
- [23] Neven, D., De Brabandere, B., Georgoulis, S., Proesmans, M., Van Gool, L.: Towards end-to-end lane detection: an instance segmentation approach. In: 2018 IEEE intelligent vehicles symposium (IV). pp. 286–291. IEEE (2018)
- [24] Pan, B., Sun, J., Leung, H.Y.T., Andonian, A., Zhou, B.: Cross-view semantic segmentation for sensing surroundings. *IEEE Robotics and Automation Letters* **5**(3), 4867–4873 (2020)
- [25] Pan, X., Shi, J., Luo, P., Wang, X., Tang, X.: Spatial as deep: Spatial cnn for traffic scene understanding. In: *Proceedings of the AAAI Conference on Artificial Intelligence*. vol. 32 (2018)
- [26] Phillon, J., Fidler, S.: Lift, splat, shoot: Encoding images from arbitrary camera rigs by implicitly unprojecting to 3d. In: *European Conference on Computer Vision*. pp. 194–210. Springer (2020)
- [27] Qin, Z., Wang, H., Li, X.: Ultra fast structure-aware deep lane detection. In: *European Conference on Computer Vision*. pp. 276–291. Springer (2020)
- [28] Qu, Z., Jin, H., Zhou, Y., Yang, Z., Zhang, W.: Focus on local: Detecting lane marker from bottom up via key point. In: *Proceedings of the IEEE/CVF Conference on Computer Vision and Pattern Recognition*. pp. 14122–14130 (2021)
- [29] Redmon, J., Divvala, S., Girshick, R., Farhadi, A.: You only look once: Unified, real-time object detection. In: *Proceedings of the IEEE conference on computer vision and pattern recognition*. pp. 779–788 (2016)
- [30] Reiher, L., Lampe, B., Eckstein, L.: A sim2real deep learning approach for the transformation of images from multiple vehicle-mounted cameras to a semantically segmented image in bird’s eye view. In: 2020 IEEE 23rd International Conference on Intelligent Transportation Systems (ITSC). pp. 1–7. IEEE (2020)
- [31] Tabelini, L., Berriel, R., Paixao, T.M., Badue, C., De Souza, A.F., Oliveira-Santos, T.: Polylandenet: Lane estimation via deep polynomial regression. In: 2020 25th International Conference on Pattern Recognition (ICPR). pp. 6150–6156. IEEE (2021)
- [32] Tian, Z., Shen, C., Chen, H., He, T.: Fcos: Fully convolutional one-stage object detection. In: *Proceedings of the IEEE/CVF international conference on computer vision*. pp. 9627–9636 (2019)
- [33] Yoo, S., Lee, H.S., Myeong, H., Yun, S., Park, H., Cho, J., Kim, D.H.: End-to-end lane marker detection via row-wise classification. In: *Proceedings of the IEEE/CVF Conference on Computer Vision and Pattern Recognition Workshops*. pp. 1006–1007 (2020)
- [34] Zheng, T., Fang, H., Zhang, Y., Tang, W., Yang, Z., Liu, H., Cai, D.: Resa: Recurrent feature-shift aggregator for lane detection. In: *Proceedings of the AAAI Conference on Artificial Intelligence*. vol. 35, pp. 3547–3554 (2021)
- [35] Zhou, X., Wang, D., Krähenbühl, P.: Objects as points. *arXiv preprint arXiv:1904.07850* (2019)